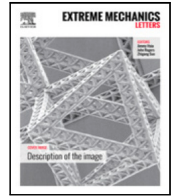




Contents lists available at ScienceDirect

Extreme Mechanics Letters

journal homepage: www.elsevier.com/locate/eml

The anti-dogbone: Evaluating and designing optimal tensile specimens for deep learning of constitutive relations

Chi-Huan Tung^{a,c}, Ju Li^{a,b,*}^a Department of Nuclear Science and Engineering, Massachusetts Institute of Technology, 77 Massachusetts Avenue, Cambridge, 01239, MA, USA^b Department of Materials Science and Engineering, Massachusetts Institute of Technology, 77 Massachusetts Avenue, Cambridge, 01239, MA, USA^c Department of Materials Science and Engineering, National Tsing Hua University, 101 Sec 2 Kuang Fu Rd., Hsinchu, 300044, Taiwan

ARTICLE INFO

Keywords:

Tensile specimen
 Constitutive relations
 Finite element method
 Machine learning
 Neural networks
 Digital image correlation

ABSTRACT

Traditional tensile testing with “dogbone”-shaped specimen (ASTM E8, first standardized in 1924) strives for strain uniformity. Multiple tests with such samples help fit simple constitutive relation parameters on real materials. With the development of deep learning, the concept of employing entirely data-driven constitutive relations to capture more intricate material behavior has arisen. Nevertheless, these methods demand experimental data that are distributed throughout the complete stress–strain configuration space to effectively train the machine learning models. This is particularly crucial for mechanisms like hardening, which are time-dependent and sensitive to loading history. In this work, we investigate the potential to efficiently gather a wider range of experimental data points in the stress–strain configuration space using non-uniform samples and displacement-field mapping, leveraging advancements in computer vision techniques. We developed a metric to quantify stress state diversity in 2D tensile experiments and used it to optimize the shape of the sheet sample. The goal was to increase stress–strain diversity obtained within a single test, particularly in the linear elastic regime. Additional geometric constraints can be introduced on the design features, considering factors such as size and curvature to adapt to the microstructural characteristics of the sample material.

1. Introduction

Tensile testing is one of the fundamental experimental techniques to measure the mechanical properties of engineering materials [1]. With standardized specimen geometry and experimental protocols, the mechanical properties of different materials can be compared quantitatively. The typical “dogbone” tensile specimen [2] consists of enlarged shoulders on both ends, gripped by the tensile tester, and a gauge section with a reduced cross-section in which the plastic deformation, damage and mechanical failure are localized. The purpose of such a sample design is to ensure a controllable and uniform uniaxial tensile deformation condition within the gauge section [3]. By stretching the sample on both ends, the material starts to deform and eventually yields upon exceeding the elastic limit, and the stress–strain curves obtained from tensile experiments give us data about the constitutive relations governing the mechanical behaviors [4–6]. Constitutive relations are of the utmost importance in materials applications because they can be applied to numerical simulations and predict the mechanical behavior in different structures or during various manufacturing processes. However, fully determining the constitutive relation of a material requires

the input of the mechanical responses under a variety of loading conditions, not only uniaxial stretching [7–9], which is laborious in general and expensive to achieve in conventional tensile testing setup.

Supervised machine learning approaches have found extensive use in modeling [10–12] and simulating [13,14] the non-linear material behaviors. Particularly, several works propose the use of a framework combining Finite Element Method (FEM) and Neural Networks (NNs). In this framework, the idea is to take the mechanical responses obtained from FE simulations as the training sets to refine the NN functions that served as the numerical replacements of the real constitutive relations [15–17]. The displacement fields calculated by FEM based on the NN functions are compared with the ground truth to iteratively refine the NN functions representing the constitutive relation. In this framework, the ground-truth data can be replaced by the one obtained in mechanical experiments. This comparison is made through a loss function, which is often the Euclidian norm of the difference between the nodal positions calculated with the NN and the ones given as ground truth. Since the backpropagation algorithm that updates the NN

* Corresponding author at: Department of Nuclear Science and Engineering, Massachusetts Institute of Technology, 77 Massachusetts Avenue, Cambridge, 01239, MA, USA.

E-mail address: liju@mit.edu (J. Li).

<https://doi.org/10.1016/j.eml.2024.102157>

Received 13 February 2024; Accepted 12 April 2024

Available online 6 May 2024

2352-4316/© 2024 Elsevier Ltd. All rights reserved.

is driven by the gradient of the loss function with respect to the NN parameters, sufficient data sets are needed to explore the variations of this loss function, or the NN could not be reshaped properly to represent the real constitutive relations. To adequately train the NN model, which expresses the material behavior in detail, a rich diversity of stress–strain paths is required. However, the only data stored in conventional tensile experiments with dogbone specimens are the total uniaxial strain and the load applied to the specimen. In addition to reading the cross-head displacement, digital image correlation (DIC) is another technique that can be used with mechanical tests to collect the full-field information of materials deformation [18]. By comparing the image between two different stages during testing, the spatial distribution of displacements and, thus, strains on the testing sample can be extracted, which can serve as a cheap yet rich source of mechanical response data. The displacement field measured by DIC is stored with spatial resolution. Therefore, the results can be interpolated and matched to the FEM-NN simulations result in order to assess the reliability of the constitutive relation within a wider subset of the phase space if the stress/strain fields are heterogeneous. Already many examples show that, in general, NNs have very good performance for interpolation, but they are extremely inaccurate for extrapolation [19–21]. In order to train the NN function to satisfactorily capture the characteristics of the constitutive relation, the designed sample geometry must allow for the generated data to cover the whole range of interest in the stress configuration space thoroughly. It has been a common practice to modify the geometry by cutting out flat sheet samples in order to introduce stress concentrations and investigate the mechanical properties [22–26]. It has also been confirmed that DIC can effectively capture the inhomogeneous deformation states within an irregularly shaped sample [26]. Creating a modified tensile specimen with an irregular gauge section would therefore be a meaningful approach for efficiently obtaining the training data for NNs with a wider range of strain and stress states.

In this work, a quantitative metric has been proposed based on the distributions of stress states in the vector space of the combinations of their normal and shear stress components to measure the diversity of stresses explored within the specimen under tension. The FE simulations on various sample geometries to obtain their stress paths and calculate the corresponding diversity metrics. Some specific sample geometries were identified to exhibit an almost uniform exploration of the stress configuration space in a single test under uniaxial tension. These observations provided a guideline to improve the tensile sample designs for extracting the information satisfying the needs of FEM-NN model training to learn constitutive relations. Then, our stress diversity score has been used in optimization algorithms (Grey Wolf Optimizer, GWO, presented here) to provide optimized sample designs. Furthermore, our method can be generalized to designing optimal samples for more specific materials, by refining the constitutive relation used during the optimization and adding geometrical constraints depending on microstructural characteristics. With an extension of the score to 3D, an equivalent method could be used for 3D sample design optimization for Digital Volume Correlation (DVC)-based experiments.

2. Theory

2.1. A stress diversity score: quantifying specimen quality

This section presented the quantitative measuring of the diversity of stress states reached by a specimen subjected to a tensile test. Fig. 1(a) illustrates a standard uniaxial tensile testing configuration applied to a thin sheet material with arbitrary geometry. Unlike the uniform gauge section design in the typical dogbone sample, these irregularities induce stress and strain heterogeneity during tensile experiments. The quality assessment of the samples was based on the following assumptions:

- Infinitesimal strain ($\|\underline{\nabla}\underline{u}\| \ll 1$, where \underline{u} is the displacement field) to describe the beginning of the stretching process.

- Plane stress in the (x, y) plane (thin sheet samples), where y is along the axis of the tensile testing machine, to correspond to DIC experiments.

These assumptions carry significant implications. In real-world experiments, it is common to encounter tests involving strains beyond the infinitesimal, and practical situations may involve buckling. Plane stress assumptions may not deviate from the actual state of the sample. However, motion out of the plane cannot be captured by a simple 2D-DIC setup, which would also be a concern for real experiments. The expandability of this study to consider 3D sample design and DVC experiments coupled with FEM-NN frameworks can be found in Section 5.

The stresses will therefore be represented by the following symmetric second-order tensor in a particular subspace containing only the in-plane components:

$$\underline{\underline{\sigma}} \equiv \begin{pmatrix} \sigma_{xx} & \tau \\ \tau & \sigma_{yy} \end{pmatrix}$$

Recall that the symmetry of this tensor comes from the conservation of angular momentum [27]. In this representation, there are three independent variables σ_{xx} , σ_{yy} and τ . Therefore, the stress state at each point can be represented by a unique three-dimensional tuple $(\sigma_{xx}, \sigma_{yy}, \tau)$.

Instead of studying the stress states reached in the full space, the discussion focus on only the diversity of stress states in the **plane** $\left(\frac{\sigma_{xx}-\sigma_{yy}}{2}, \tau\right)$, often called the “ π -plane” or “deviatoric stress plane” [28]. Note that the combination $\frac{\sigma_{xx}+\sigma_{yy}}{2}$, which stands for hydrostatic pressure within the subspace of in-plane stress components, evolves perpendicularly to this plane. Indeed, in a number of materials, the hydrostatic pressure has a small influence on the yielding behavior [29]. This applies to all materials exhibiting behavior that approximates a perfect plasticity law, where the deviatoric stress tensor $\underline{\underline{s}} = \underline{\underline{\sigma}} - \frac{1}{2}\text{tr}(\underline{\underline{\sigma}})$ dominates [30]. Such a framework is useful for simplifying the representation of stress diversity. To show what this simplification corresponds to, Fig. 1(b) shows the evolution of $(\sigma_{xx}, \sigma_{yy}, \tau)$ in each element of a FEM specimen during a tensile test. The projection of cylindrical yield surface in the plane of $\left(\frac{\sigma_{xx}-\sigma_{yy}}{2}, \tau\right)$ is a perfect circle in Fig. 1(c). This type of isotropic yielding behavior has already been learned by neural network [16,17]. Similarly, this concept can be extended to learn an anisotropic relationship, where exploring the yield surface from various directions is necessary.

Given that there was no prior information available about the plastic behavior of the material under study before experimentation, this study primarily concentrated on assessing sample quality based on results derived from linear elastic behavior. Linear elasticity is computationally efficient and serves as a representative model for materials at low strains, making it a practical choice for assessing how sample geometry influences the diversity of stress–strain states. Evidenced by Fig. 1(b–c), the elastic behavior provides approximate information on the directions towards the yield surface taken by the stress states in the stress space, at each point of the sample. In such a case, the intensity of the applied force or displacement on the boundary Ψ acts only as a multiplicative factor on the stress and strain fields in Ω . Therefore, only the initial directions taken by stress state points in the π -plane are examined.

The red dots in Fig. 1(c) shows the stress states under external strain $\epsilon = 0.1\%$. At this strain level, an approximated linear elastic behavior was observed. These stress states start to depart from the origin radially once the sample is stretched. The stress states were normalized by the maximum von Mises effective stress $\sigma_{\max} = \max\left(\sqrt{\frac{3}{2}\underline{\underline{s}} : \underline{\underline{s}}}\right)$ as displayed in the inset of Fig. 1(d). In this plane, $\left(\frac{\sigma_{xx}-\sigma_{yy}}{2}, \tau\right)$ can be transformed into polar coordinate (r, ϕ) where $r = \sqrt{\left(\frac{\sigma_{xx}-\sigma_{yy}}{2}\right)^2 + \tau^2}$ and $\phi = \text{atan2}\left(\tau, \frac{\sigma_{xx}-\sigma_{yy}}{2}\right)$, where the angle

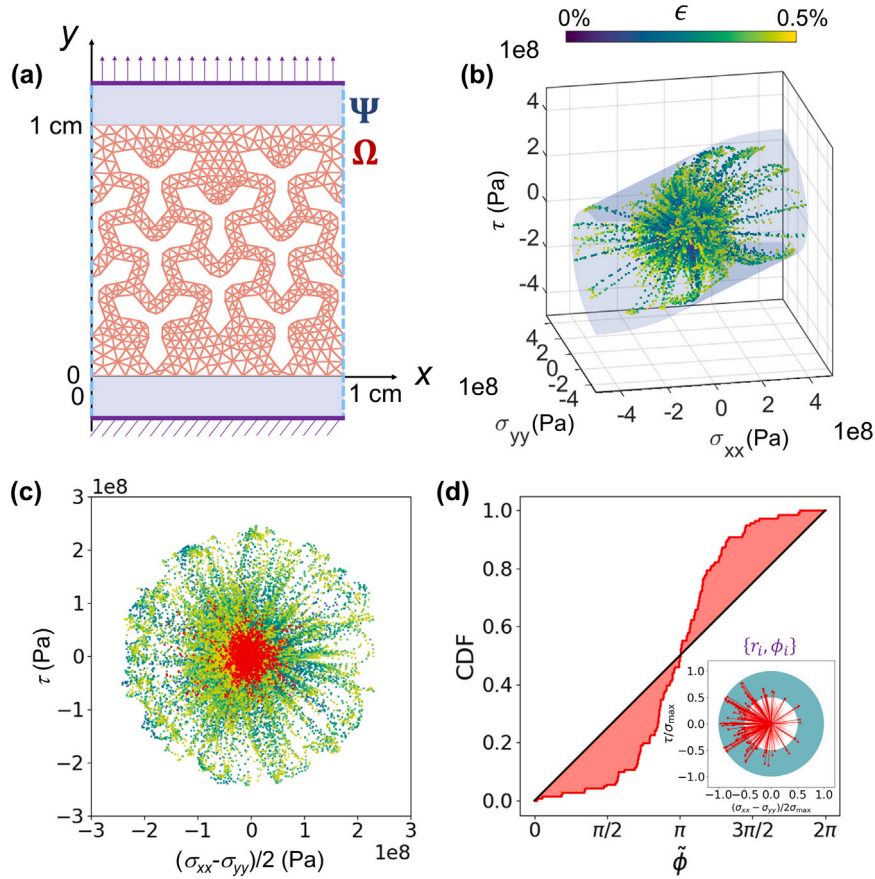


Fig. 1. Numerical metric measuring a sample quality based on its stress states. (a) The example FEM sample mesh. The Dirichlet boundary conditions are shown in purple and the free boundaries are represented by blue dashed lines. (b) Stress states of each mesh element in the space of stress components $(\sigma_{xx}, \sigma_{yy}, \tau)$ assuming perfect plasticity until applied strain $\epsilon = 0.5\%$, the yielding surface is indicated by blue isosurface. (c) Stress states in the plane $(\frac{\sigma_{xx}-\sigma_{yy}}{2}, \tau)$, the stress states at applied strain $\epsilon = 0.1\%$ are marked as red dots. (d) Example of the cumulative circular distribution of the stress states displayed in panel (c), the deviation between the cumulant (red curve) and that of a uniform distribution (black curve) is used to define S_{cdf} to represent the angular diversity of stress state. The inset shows stress states normalized by the maximum von Mises effective stress σ_{max} , for a simulation assuming pure elastic behavior. The data points within the range $r/\sigma_{max} \in [1 - f_{th}r_{med}, 1]$ with $f_{th} = 1$ (teal background), marked as bold red dots, are the ones used to evaluate the sample quality. (For interpretation of the references to colour in this figure legend, the reader is referred to the web version of this article.)

ϕ is related to the orientation of principal stress within the physical coordinate. This representation of the distribution of stress points is utilized to define a numerical score measuring the sample quality.

In addition to angular distribution, radius r also contains information about the sample quality. For example, considering the ultimate tensile strength of a ductile metal can be around 10 times its yield strength, before the material develops irreversible damage and breaks, the difference between maximum and minimum von Mises effective stress of the region undergoing plastic deformation is around 90% of the maximum value. In other words, only data points with $r/\sigma_{max} > 0.1$ effectively provide information about the material's plastic behavior, which is beneficial for training the NN constitutive model. To account for this in the sample quality score, we focus exclusively on data points with the highest stress radii. The threshold concerning the median of the stress radii distribution, denoted as r_{med} , was carefully selected to guarantee statistical stability across discretized data obtained from various sampling techniques and different machines, assuming the same input mesh and loading conditions. Subsequently, f_{th} was introduced as a parameter to fine-tune the data selection: stress data points with $r > f_{th}r_{med}$ were categorized as "significant" data for the purpose of learning, and only these points were retained for the calculation of the diversity score. In the inset of Fig. 1(d), the significant points, highlighted as bold red dots against the teal background, are selected based on the parameter f_{th} . This parameter allows our metric to be

versatile and applicable to a variety of material systems with different failure behaviors.

The goal was to achieve a uniform angular distribution of stress states within this π -plane. Therefore, any distributions that display clustering of data points deviating from this uniform distribution should be subject to penalties. Here the circular distribution was wrapped at $\tilde{\phi} = 0, 2\pi$, where $\tilde{\phi} = \phi - \phi_{cm} + \pi$, and ϕ_{cm} is the circular mean of stress states defined as $\phi_{cm} = \text{atan2}(\langle \sin \phi_i \rangle, \langle \cos \phi_i \rangle)$. We defined S_{cdf} as the integral

$$S_{cdf} = \frac{6}{\pi} \int_0^{2\pi} (r(\tilde{\phi}))^2 d\tilde{\phi} \quad (1)$$

in terms of the residual $r(\tilde{\phi}) \equiv c(\tilde{\phi}) - \frac{\tilde{\phi}}{2\pi}$, and the cumulant $c(\tilde{\phi}) \equiv \frac{1}{N} \int_0^{\tilde{\phi}} \sum_{i=1}^N \delta(\phi' - \phi_i) d\phi'$ [31] in Fig. 1(d) to represent the angular diversity of stress state as displayed by the inset. Considering the perfectly isotropic distribution that all data points distributed uniformly around the circle, $c(\tilde{\phi}) = \frac{\tilde{\phi}}{2\pi}$ and therefore $S_{cdf} = 0$. On the opposite extreme, the most undesired case is that most of the data points are perfectly aligned in the same direction. In such case, $c(\tilde{\phi}) = H(\tilde{\phi} - \pi)$ and $S_{cdf} = 1$ where $H(x)$ is the Heaviside function. Note that according to Eq. (1), S_{cdf} is insensitive to the amount of data points for sufficiently large N_g , therefore the stress diversity score provide a stable metric to quantitatively compare the different angular distributions of data points.

3. Calculation

This section offers a comprehensive explanation of the process for acquiring stress state distributions and their corresponding stress diversity scores. Additionally, we will illustrate the optimization procedure used to enhance sample geometry designs and attain greater stress diversity.

3.1. Finite element tensile simulations

The 1 cm \times 1 cm square sheet patterned sample in Fig. 1(a) is subject to displacement-controlled tension along the y -axis until the total applied strain $\epsilon = 0.5\%$. Stress states are examined in elasto-plastic FE simulations using the Fenics [32] package in Python assuming perfect plasticity [33], and the mechanical properties of plain carbon steel: Young's modulus $E = 200$ GPa, yield stress $\sigma_y = 350$ MPa, and Poisson's ratio $\nu = 0.25$ [34,35]. Hence, the tensile strain at the elastic limit is $\epsilon_y = 0.175\%$. The stress and strain states on the FEM mesh vertices were subsequently interpolated to a uniform grid that corresponds to the sample area. This ensures uniform sampling conditions, making it compatible with the typical format of DIC datasets. In Section 4.1, we will present the results of stress state distributions and their corresponding S_{cdf} for various sample geometries.

3.2. Geometry optimization

The optimization problem can be described as follows:

$$\text{Find } \arg \min_{\rho|\Omega} S_{\text{cdf}}(\rho)$$

where $\rho : \Omega \cup \Psi \rightarrow \{0, 1\}$ represents the density of matter on the sample, Ω the space filmed by the camera in a DIC study and Ψ the rest of the sample in which the density is uniform ($\rho|\Psi = 1$). The notations correspond to those in Fig. 1(a). To simplify this problem, the approach involves seeking an approximation of its solution within specific function subspaces of Ω in $\{0, 1\}$.

Algorithm 1: Geometric Optimization Algorithm. This iterative process starts with parameterized model ω and initial guesses λ_i . At each iteration, it generates a mesh, conducts FE simulations for stretching, and calculates S_{cdf} based on the obtained data. The GWO updates λ to minimize S_{cdf} . After completing a set number of iterations, the optimal parameters λ_{opt} are selected. Finally, the optimized sample geometry Ω_{opt} is obtained by evaluating the model with λ_{opt} : $\Omega_{\text{opt}} \equiv \omega(\lambda_{\text{opt}})$.

Input: Parametric models ω with inputs λ , initial guesses λ_i
Result: $\Omega_{\text{opt}} \equiv \omega(\lambda_{\text{opt}})$

```

1  $\Omega \leftarrow \omega(\lambda_i)$ 
2  $i \leftarrow 0$ 
3 while  $i < \text{Maxiter}$  do
4   Evaluate stress states  $(\sigma_{xx}, \sigma_{yy}, \tau)$  in FE simulation.
5   Evaluate  $S_{\text{cdf}}$  from the stress states.
6   Update  $\lambda$  with GWO algorithm to minimize  $S_{\text{cdf}}$ .
7    $i \leftarrow i + 1$ 
8 end
9  $\lambda_{\text{opt}} \leftarrow \lambda$ 
10 return  $\Omega_{\text{opt}} \equiv \omega(\lambda_{\text{opt}})$ 

```

To simplify calculations and account for geometric constraints to avoid undesirable shapes, we have developed several parametric sample models. Detailed descriptions of these models are available in Appendix B. The global optimization algorithms were employed using the NEORL library [36] to discover the parameter combinations that yield the sample with the lowest fitness. In our case, the fitness metric to minimize is S_{cdf} . The optimization procedure is outlined in Algorithm 1. This algorithm generates the mesh corresponding to

the parameters λ , conducts FE simulations of tensile stretching, and computes S_{cdf} for the obtained data points. The parameters λ are then iteratively updated by the optimizer to minimize S_{cdf} . The optimizer was achieved by GWO algorithm [37]. Based on the population-based meta-heuristic algorithm, replicas of mutated parameters are updated iteratively according to their previous positions in the search space. These replicas share information with each other and organize their movements by mimicking the hunting behavior of wolf packs. Conventional multivariable global optimization techniques such as stochastic gradient descent and its variants [38] could potentially offer advantages in terms of computational efficiency. However, the approach we chose had the benefit of not necessitating the evaluation of gradients for minimizing objectives. This is particularly advantageous in various situations, especially when complex FE simulations and interpolations are needed to compute S_{cdf} , making gradient calculations unfeasible.

4. Results

4.1. Numerical evaluation of 2D tensile specimens

The stress diversity score defined in the previous section is now employed to evaluate the performance of different sample geometries. By creating holes of different sizes, shapes and arrangements, heterogeneity was introduced in the 1cm \times 1cm¹ square sheet sample with isotropic and uniform elastic properties. The stress states were collected in each mesh element under elastic deformation in the FE simulations described previously to evaluate the sample quality, with $f_{\text{th}} = 1$.

Fig. 2 displays several sample designs along with their stress states for a linear elastic behavior. Spatial distributions of r and ϕ are visualized as pseudocolor plots to emphasize that, in this work, the diversity of stress states is a consequence of the heterogeneous full-field deformations. Such diversity can be captured by image processing techniques such as DIC. We can either interpolate the FEM stress data to random sample points with uniform distributions or regularly-spaced grid of sampling points in Ω while excluding the ones in holes to eliminate the effect of heterogeneity in FEM mesh density when comparing between different sample designs.

Panel (a)–(c) display the stress states of a sample with no hole/notch in the gauge region. In this case, there is no stress heterogeneity within the sample and $S_{\text{cdf}} = 1$, indicating that all stress data points are perfectly aligned. This is exactly the condition people will generally look for and find in the gauge section of traditional “dogbone” shaped specimens. Unfortunately, it is also the most undesired pattern for FEM-NN data analysis framework.

A simple yet straightforward way to introduce stress heterogeneity to testing is by introducing holes in the sample [16,17]. As demonstrated in **panel (d)–(f)**, the discrepancy between data points begins to emerge and S_{cdf} decreased to 0.85. However, most significant data points are still distributed within a $\pi/2$ sector, indicating the information that can be learned from these data points is still mainly limited to the behavior close to pure tensile stretching along the y axis.

The question arises whether it is possible to induce stress states that are very different from the uniaxial σ_{yy} tension, such as pure shear or pure tension along the x axis, by merely stretching the sample along the y axis. **Panel (g)–(i)** provided a successful example. By cutting out an array of non-convex bow tie-shaped holes, the retained parts in this sample form a network structure in which each node is bridged with its neighbor by an arch. Upon stretching the sample, these arches are straightened jointly, resulting in compressive stress in the convex side and tensile stress in the opposite. Similar behavior can also be found

¹ Different sample size could have been chosen here. It could be important to cope with geometrical constraints influenced by microstructural characteristics of the material while enabling complex hole patterns, and to correspond to the practical limitations of the sample preparation and testing tools.

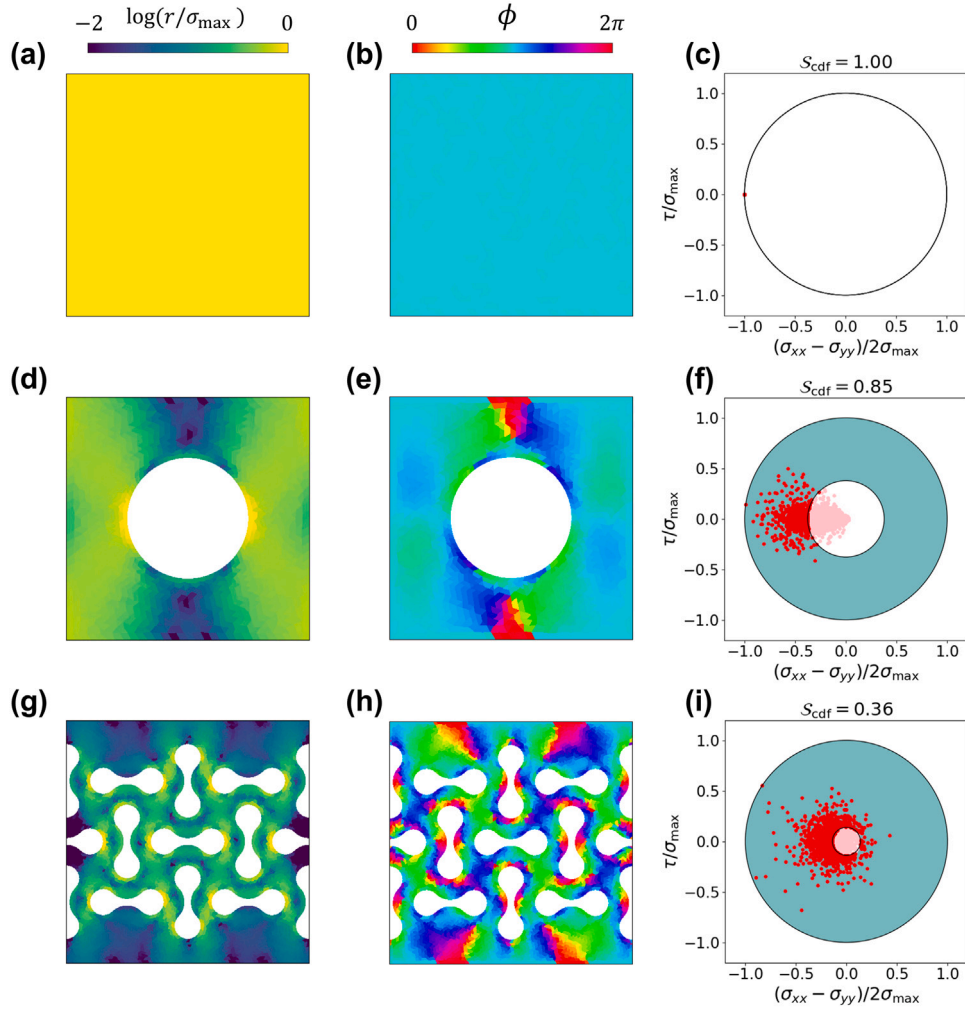


Fig. 2. Stress states in different sample geometry under linear elastic perturbations. The left and middle columns display the spatial distribution of r and ϕ respectively, and the right column demonstrates normalized stress states, with a teal background representing the relative threshold $f_{th} = 1$. (a)–(c): uniform sample without a hole. (d)–(f) single circular hole at the center. (g)–(i) network structure with bowtie-shaped non-convex holes.

in auxetic patterned structures [39]. Therefore, the major principal stresses with different orientations were generated by configuring the directions of these arches. As displayed in Fig. 2(h) we obtained a great diversity of ϕ ranging from 0 to 2π in the different parts of our sample. The resulting stress paths are displayed in Fig. 2(i), S_{cdf} is further reduced to 0.36, and the distribution of significant data points marked by bold dots is more isotropic in the π -plane than the above cases.

Fig. 3 displays the stress diversity of more different sample designs, where the S_{cdf} are plotted against f_{th} to demonstrate how the stress diversity score changes with the threshold determining whether the collected stress states are significant. The corresponding stress state distributions are provided in the appendix Fig. A.6. By lowering the f_{th} , we incorporate more data points into the calculation of stress diversity, including more directions that are considered to be “explored”, and S_{cdf} decreases. All the sample designs exhibit different degrees of stress diversity, except the uniform sample without a hole. The legends are sorted according to S_{cdf} at $f_{th} = 1$ in descending order.

At this threshold value, the S_{cdf} of those patterned samples can be categorized into two groups. The sample designs with simple or no holes display less uniform stress state distributions in the π -plane, whereas the ones with an array of complex holes display more stress diversity. This is because in the structure with a single convex hole, uniaxial stretching along the y -axis creates greater von Mises effective stress on the left and right of the hole due to the reduction of

supporting area, and the plasticity usually develops in this left and right sides of the hole. However, in these regions, the orientations of principal tensile stresses are aligned with the y -axis as indicated by the cyan color in Fig. 2(e), resulting in insufficient plasticity data about the horizontal stretching along x -axis in these samples. In contrast, as displayed in Fig. 2(g)–(i), by properly arranging the non-convex holes, those retained arch-like structures in different orientations are straightened cooperatively. S_{cdf} of these samples is reduced to less than 0.2, indicating that they could be copious sources of data for neural network training.

Judging from the S_{cdf} at different f_{th} , Fig. 3 is also a useful instruction for selecting the sample design for the materials with different level of ductility. When studying a brittle material or focusing solely on shallow plasticity, the sample design with the lower S_{cdf} may be chosen at higher f_{th} for only a small fraction of stress states approaching the yield surface. Whereas if the goal is to study the material behavior under deep drawing, consideration may also be given to the samples with low f_{th} that incorporate more data points.

4.2. Geometry optimization

Based on a quantifiable measure of sample quality, we suggest an approach to generate improved sample geometry through the utilization of optimization algorithms. Parametric models, including Bézier

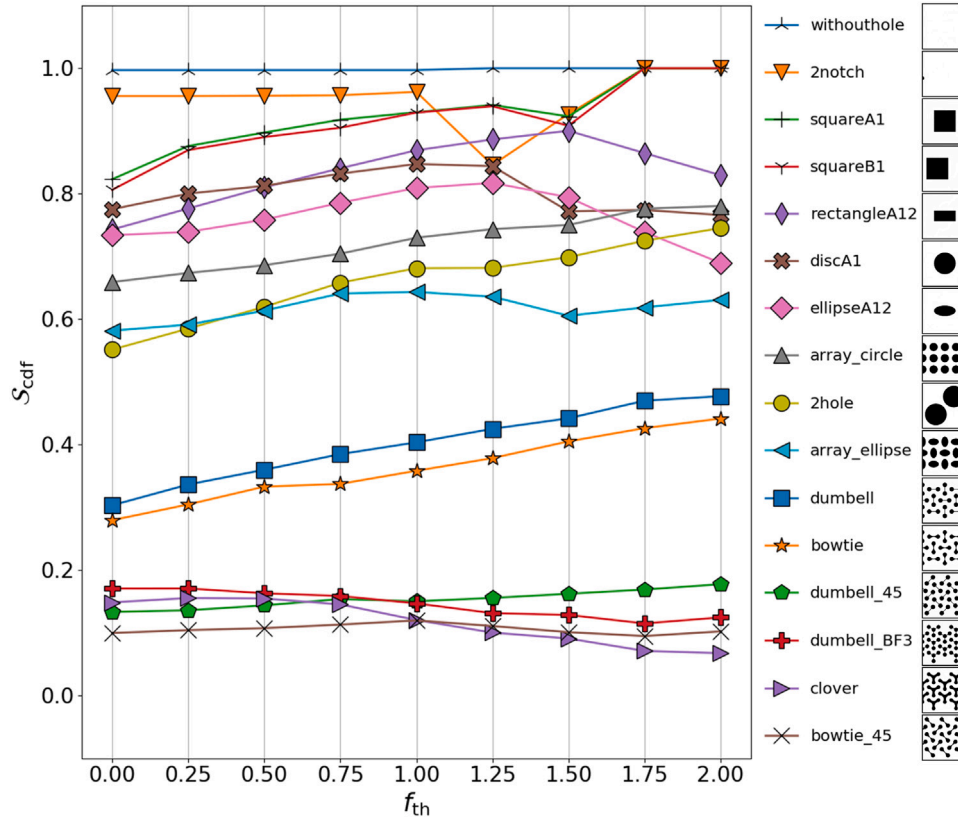


Fig. 3. Stress diversity score map. S_{cdf} of various sample with the relative threshold = [0.00, 0.25, 0.50, 0.75, 1.00, 1.25, 1.50, 1.75, 2.00], respectively. The legend is ordered according to the score at $f_{th} = 1.00$ in descending order.

2-fold/3-fold symmetric models and the free harmonic holes (FHH) model, were selected to streamline the optimization process by limiting the number of degrees of freedom that are permitted to vary. Their construction is presented in Appendix B. The first two are inspired by the best geometries referenced in Fig. 3, with an array of holes showing 2-fold or 3-fold symmetry. The FHH model offers a greater degree of freedom, allowing the exploration of more varied hole geometries and positions, while the number of holes is constrained. Since now S_{cdf} can be computed as a function of a tuple of parameters with defined bounds and data types, the optimizing problem now becomes straightforward. In addition, the constraints on parameter bounds can also be informed by microstructure considerations and practical limitations related to sample preparation.

In Fig. 4, we present GWO optimization results for three different parameterized models. For each sample, the spatial stress distribution is displayed in the two first columns, the first one representing the r distribution and the second one the ϕ distribution. This representation of the stress states with polar coordinates has been explained in Section 2.1. The last column contains the representations of the stress states in the π -plane. Appendix Table C.1 contains the detailed model parameters of the optimized samples with their calculated stress diversity score. It also displays the hyperparameters used for GWO, including the optimization space and the number of wolves used, which corresponds to the number of configurations tested in each generation, as well as the number of generations. The results confirm that remarkable stress diversity scores can be achieved with very simple optimized models. Evidenced by Fig. 4(c) and (f), the stress points are distributed in an almost isotropic manner. It is particularly manifested in the Bézier symmetric models, which only require 3 or 4 parameters, because the knowledge acquired in Section 4.1 has been well exploited. Furthermore, those fixed holes models enable us to prevent the convergence towards the geometries that could not easily be made in practical tests. Although it attains a higher stress diversity score, the outcome from the

free harmonic hole model is particularly intriguing. It shows that the holes with unrestricted geometries have a tendency to merge, yet they remain separated by very thin strips connecting the upper and lower sections of the sample. Such a pattern avoids creating large continuous zones that would almost only undergo a uniform uniaxial tension along the y axis. Unfortunately, these thin strips may pose certain challenges. Specifically, the evolution of the stress field within these narrow linking bonds, which is exactly the source of stress diversity, could potentially result in breakage, even during the initial stages of deformation. It could also result in out-of-plane bending in practice, as discussed below in Section 5.

Fig. 5 shows the evolution of the best S_{cdf} identified at every generation of the three GWO jobs. The choice of models that tend to create better candidates (Bézier symmetric models) enables the optimization process to depart from already very low scores. Even without knowing whether there exists a better score in more iterations, satisfactory results are already achieved within a few generations. The outcome for the harmonic holes model (c) also demonstrates satisfactory convergence, although it is challenging to conclude that no further improvement is possible.

To conclude, this optimization process enables us to quickly reach great score diversity, and it can give lots of ideas to any experimenter or machine learning specialist interested in anisotropic constitutive law learning.

5. Discussion

An important question regarding the practical aspect of these anti-dogbone specimens is the feasibility of obtaining the strain states in DIC experiments. With the aid of numerically controlled laser cutting, the anti-dogbone samples can be precisely produced in the laboratory on thin sheet materials. However, if one tries to stretch the sample following the boundary conditions indicated in Fig. 1(a), deviations from 2D

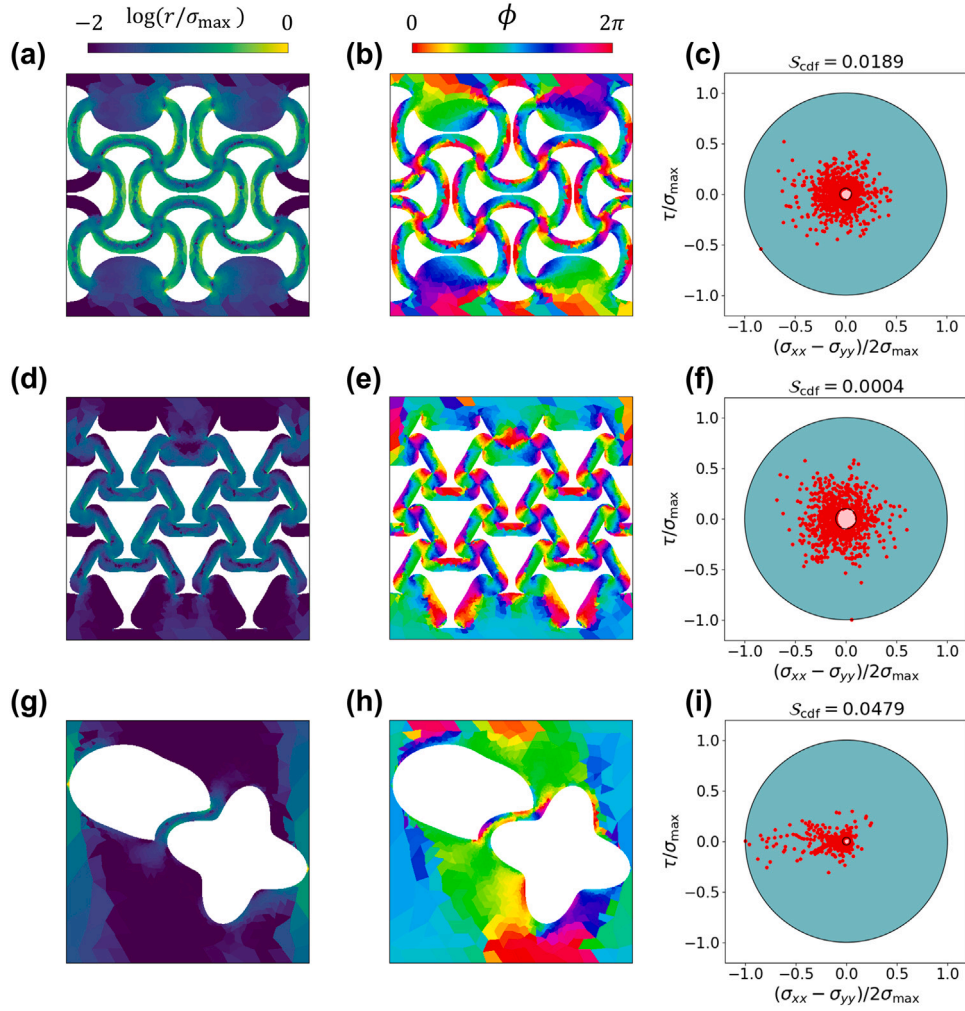


Fig. 4. Stress states in the optimized samples based on parameterized models. The left and middle columns display the spatial distribution of r and ϕ respectively (polar coordinates in the π -plane defined previously), and the right column demonstrates normalized stress states, with a teal background representing the threshold $f_{th} = 1$. (a)–(c): 2-fold symmetrical hole array. (d)–(f) 3-fold symmetrical hole array. (g)–(i) free harmonic holes.

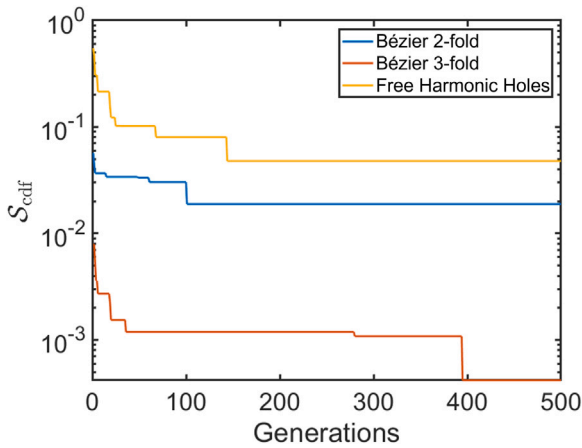


Fig. 5. S_{cdf} returned during GWO optimization process.

FEM simulation predicted deformation conditions may emerge. Such a deviation is generally due to out-of-plane bending created under non-uniform strain states. The presence of such instability can already be well predicted by the instability criteria based on the in-plane linear elastic responses [40,41]. This discrepancy arising from out-of-plane

deformations may be minimized by taking into account the in-plane elastic instability along with S_{cdf} during geometry optimization. In the meantime, experimental studies are needed to check the quality of the designs obtained with these 2D assumptions for DIC in a machine learning of constitutive relation experiment in practice. Another concern arises that the DIC approach could often omit pixels around sample edges. To handle this, modifications can be applied by either excluding data points that DIC could not access in terms of their distances from the edges, or including a corresponding penalty term into the loss function to account for these missing data points.

While practical 2D studies might be challenged by the occurrence of out-of-plane behavior, our approach represents an initial step towards prospective 3D investigations. Indeed, full-field measurement techniques including tomography scans [42] or confocal imaging [43] could also be used for DVC for 3D samples, and similar neural network training processes could be designed to acquire the full 3D behavior of materials. For such applications, our approach could be generalized to 3D sample optimization, with an extension of the stress diversity score to a 3D stress tensor.

The exploration of how sample geometry can enhance the information density for NN training contributes to the continuous refinement of sample design. Given that the loss function for training NN typically involves the summation of stress, strain, or displacement deviations from each DIC pixel, we suggest incorporating data point density into the target function to be optimized in future studies. Additionally,

to comprehensively capture mechanical properties across all potential directions, the requisite number of experiments for a “dogbone”-shaped specimen will decrease inversely with the required angular resolution or bin width. Adequate data points within each angular bin are therefore crucial for obtaining dependable statistics. Eq. (1) conveniently expresses the deficiency of a particular sample geometry in comparison to one that produces an ideal isotropic stress distribution. Notably, Eq. (1) can be modified to delineate differences in the data richness from two different sample geometry Ω_p and Ω_q by:

$$S_{p,q} = \frac{6}{\pi} \int_0^{2\pi} (c_p(\hat{\phi}) - c_q(\hat{\phi}))^2 d\hat{\phi}, \quad (2)$$

where c_p and c_q corresponds to the cumulant from Ω_p and Ω_q .

Moreover, the proposed method can be adjusted for designing tensile specimens to learn more specific material behaviors within an iterative framework. If an approximate stress–strain relation is already known, it can be utilized in a FE simulation to calculate a behavior-specific stress diversity score. Sample optimization can be performed using this initial approximated relation, and the resulting sample can then be used to refine the constitutive relation. It is important to acknowledge that material behavior can often be highly nonlinear due to factors like work hardening, thermo-mechanical coupling, or damage accumulation. In such cases, relying solely on infinitesimal strain approximations may be limited. Once the qualitative behavior of material plasticity is understood within a specific material system, the FE simulation routine can be adjusted to replicate any necessary phenomena that affect strain development in stress/strain states. By making these modifications, optimal sample designs can be developed to capture information in the deeper plastic stages of material behavior.

6. Conclusions

In this work, several sample geometries were proposed to be able to produce complex stress states in tensile experiments. These sample designs provide fruitful sources of training data for NNs to capture the mechanical properties, which are generally inaccessible by the standard dogbone specimens. Since most of the commonly used mass production processes such as rolling, drawing or extrusion will produce anisotropic textures in material, it is also worthwhile to consider which sample designs could lead to a more thorough exploration of stress states in mechanically anisotropic materials. The geometry optimization algorithm, relying on parameterized models, offers flexibility in addressing the anisotropy. It allows for obtaining optimized sample geometries capable of presenting diverse data for NN training by minimizing S_{cdf} based on stress states derived from anisotropic FE simulations.

The score design and optimization tasks have been proposed based on the concept that an ideal elastic behavior would represent many material responses at low strains. It would be interesting to take some of the optimized designs and compare the π -plane stress plots obtained with DIC during tensile stretching experiments and the ones returned by elastic FE simulation. Additionally, comparing their S_{cdf} at low strain would be meaningful if sufficient image precision can be achieved at this stage of the experiment. To tailor the optimization process for specific materials and not solely rely on the design provided for linear elastic behavior, one might consider an iterative optimization approach that involves refining both the constitutive relation and the sample design alternately.

Enhancing NN performance for learning anisotropic constitutive relations is undoubtedly valuable. However, it is worth noting that the low extrapolation performance of NNs implies that conducting numerous experiments with simple dogbone samples would be necessary, which could substantially extend the time and material resources required. Therefore, the optimal sample geometry proposed in this work has the potential to address this challenge effectively. This work underscores the significance of innovative approaches at the intersection of materials science, optimization, and machine learning in shaping the future of mechanical characterization and design.

Code availability

The computer codes used for simulations and analyses are available from the corresponding author upon request.

CRediT authorship contribution statement

Chi-Huan Tung: Conceptualization, Data curation, Formal analysis, Investigation, Methodology, Software, Validation, Visualization, Writing – original draft, Writing – review & editing. **Ju Li:** Conceptualization, Funding acquisition, Investigation, Methodology, Project administration, Supervision, Writing – original draft, Writing – review & editing.

Declaration of competing interest

The authors declare that they have no known competing financial interests or personal relationships that could have appeared to influence the work reported in this paper.

Data availability

Data will be made available on request.

Acknowledgments

We gratefully acknowledge Aurélien Legoupil for his valuable discussions and keen interest, which have greatly enriched this work. J.L. acknowledges support by the Laboratory Directed Research & Development Program at Idaho National Laboratory, USA under the Department of Energy (DOE) Idaho Operations Office (an agency of the U.S. Government) Contract DE-AC07-05ID145142. C.-H.T. acknowledges support from Graduate Students Study Abroad Program sponsored by the Ministry of Science and Technology (MOST), Taiwan, under Grant No. MOST110-2917-I-007-012.

Appendix A. Stress states in different sample geometry under linear elastic perturbations

See Fig. A.6.

Appendix B. Parameterized models used in topological optimizations

Bézier symmetrical patterns

We propose parameterized models in the two different types of symmetrical patterns:

- 2fold: **mm2** symmetrical holes arranged in an array of **p4gm** wallpaper group.
- 3fold: **3m** symmetrical holes arranged in an array of **p31m** wallpaper group.

where the symmetry is noted in Hermann–Mauguin notations [44,45]. Fig. B.7(a) and (b) display these patterns respectively. The symmetrical holes are generated by distorting and dilating the unit cells boundaries to width w . As displayed in Fig. B.7(c), the blue straight segments are replaced by the red Bézier curves. Here, we use n control points to determine the parameterized curve [46]. Fig. B.7(d) describes the arrangement of control points in 2fold. The black vertices on both ends were fixed, and the rest of $n - 2$ red vertices are distributed uniformly along the x -axis. Their y coordinate can be noted as $y_{-m}, y_{-m+1}, \dots, y_{-1}, y_0, y_1, \dots, y_{m-1}, y_m$. By limiting $y_m = y_{-m}$, we can use parameters: $[w, y_0, \dots, y_m]$ to describe the sample geometry. On the other hand, the control points of Bézier curves in 3fold are described in two-center bipolar coordinates (θ_x, θ_y) as displayed in Fig. B.7(e), and the parameters becomes $[w, \theta_{y0}, \dots, \theta_{ym}]$.

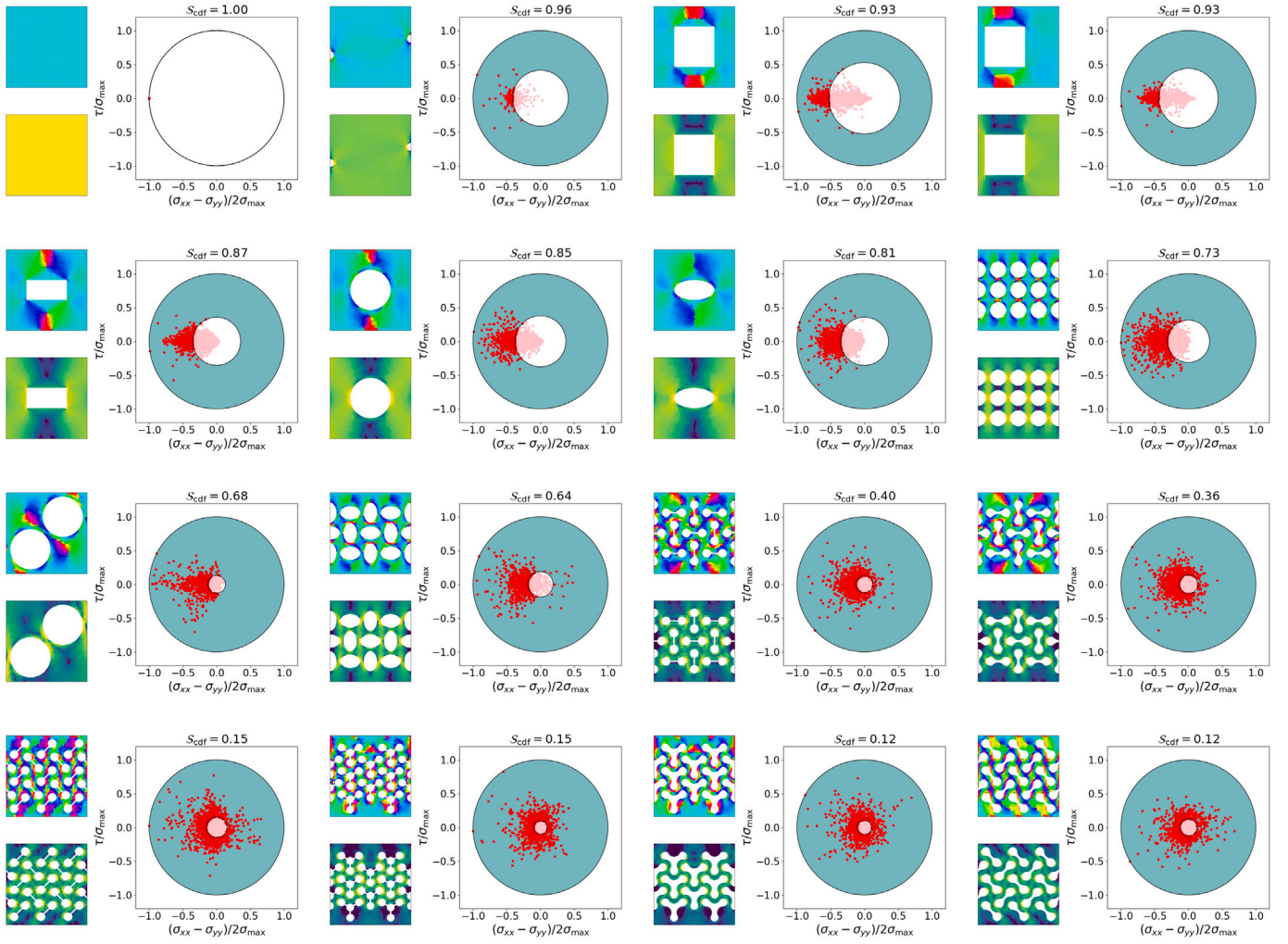


Fig. A.6. The π -plane stress states distributions for all the 16 different sample geometry displayed in Fig. 3. Spatial distributions of r and ϕ are also visualized as pseudocolor plots on the side. Panels are sorted according to their S_{cdf} at the truncation level $f_{th} = 1$.

Free harmonic holes

In order to explore sample geometries with greater disorder and more varied hole geometries, the following free harmonic hole model has been tested. Each hole is represented by its center (x, y) , an expansion coefficient R_{max} and a sequence of coefficients associated with each harmonic k (c_k, ϕ_k). In polar coordinates (R, θ) with origin (x, y) , the contour equation is:

$$R(\theta) = \frac{R_{max}}{2} \left(\frac{\sum_{k=1}^{N_h} c_k \cos(k(\theta + 2\pi\phi_k))}{\max_{\tilde{\theta} \in [0, 2\pi]} |\sum_{k=1}^{N_h} c_k \cos(k(\tilde{\theta} + 2\pi\phi_k))|} + 1 \right)$$

To avoid creating thin bands of material that would easily break, a band of material is added around the hole: its inner contour is $r_{in}(\theta) = R(\theta)$ and its outer contour $r_{out}(\theta) = R(\theta) + w$, where the width w is an optimization parameter that is usually fixed but can be released within a certain range (see Fig. B.8). The parameters are specified in the following order, with the exponent corresponding to the hole numbering and the index corresponding to the harmonic numbering: $[w, n_{holes}, x^{(1)}, y^{(1)}, R_{max}^{(1)}, c_1^{(1)}, \phi_1^{(1)}, \dots, c_{N_h}^{(1)}, \phi_{N_h}^{(1)}, c_1^{(2)}, \phi_1^{(2)}, \dots, c_{N_h}^{(2)}, \phi_{N_h}^{(2)}, \dots, c_1^{(n_{holes})}, \phi_1^{(n_{holes})}, \dots, c_{N_h}^{(n_{holes})}, \phi_{N_h}^{(n_{holes})}]$

The number of holes (n_{holes}) is fixed for the optimization, and the holes are placed one after the other in a subspace of the rectangle representing the sample. Because of the presence of w wide bands, the order of addition of the holes matters in the optimization of this model.

Appendix C. Results obtained from geometric optimization

See Table C.1.

Appendix D. Numerical stability of the stress diversity metric

To assess the numerical stability of the stress diversity metric, we considered three different specimen designs: a simple disc hole (Fig. 2 d-f), optimized hole arrays with 2-fold symmetry (Fig. 4 a-c), and the optimized free harmonic hole (Fig. 4 g-i). The stress diversity metric was evaluated for various values of f_{th} ranging from 0 to 2.0. The mesh sizes were repeatedly refined until the number of mesh cells exceeded 100,000, where the minimum feature size is around 3×10^{-4} of the sample width. For the simple disc hole and optimized 2-fold hole arrays, the stress diversity metric showed negligible differences among the different levels of mesh refinement. However, in the case of the optimized free harmonic hole specimen, the significant feature size heterogeneity resulted in varying sizes of mesh cells in different parts of the sample. As a consequence, there were gradual changes in the stress diversity metric, while the general trend remained intact. Introducing parametric limitations on the feature size in sample design can be a valuable approach to controlling the variation of mesh densities in the specimen. By carefully managing the distribution of mesh cells and considering the inherent limitations of image resolution, we can ensure accurate and reliable results in DIC analysis, particularly when dealing with challenging imaging conditions (see Fig. D.9).

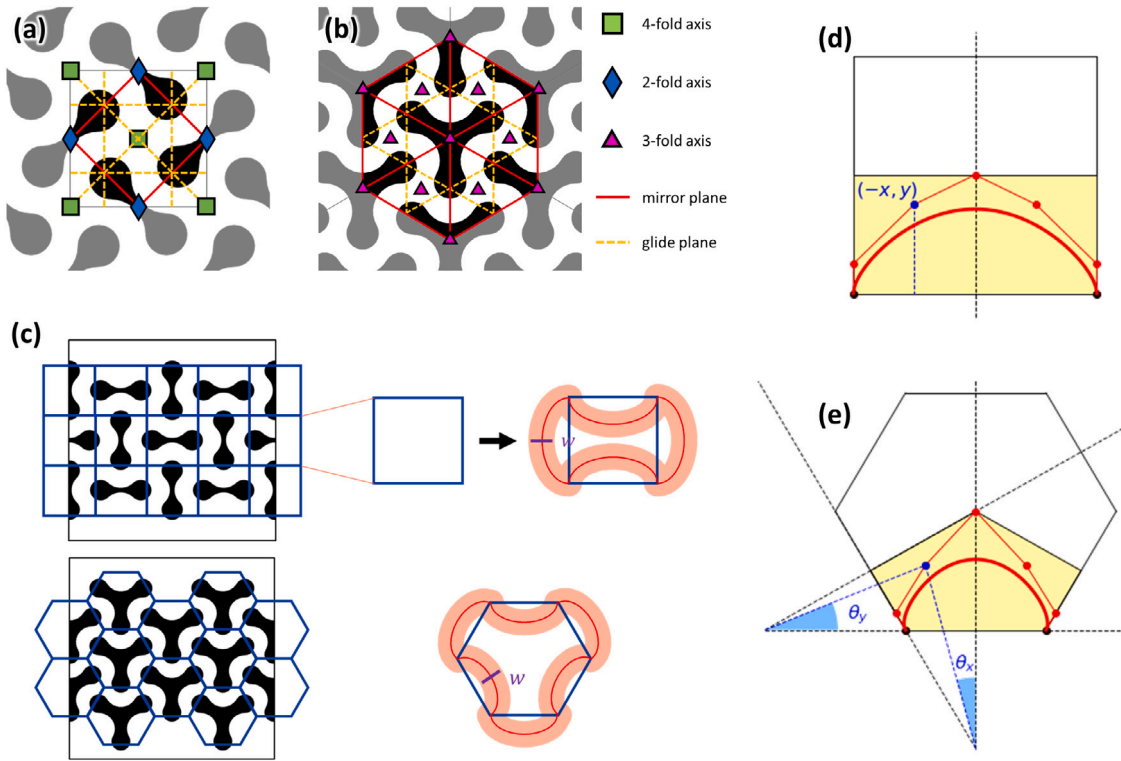


Fig. B.7. Geometric patterns used in geometry optimization (a)–(b) Schematic diagram of the 2fold and 3fold pattern. (c) Symmetrical holes are generated by replacing the unit cell boundaries (blue) with parameterized curves (red). (d)–(e) Bézier curves and their control points used to determine the distorted unit cell boundaries in panel (c). (For interpretation of the references to color in this figure legend, the reader is referred to the web version of this article.)

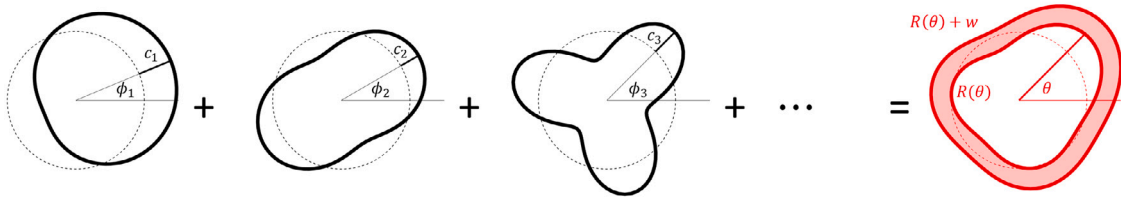


Fig. B.8. Free Harmonic Holes Parameterized hole pattern where the hole shapes are defined by superposition of harmonic functions.

Table C.1

Parameters used for Grey Wolf Optimization algorithms and results obtained.

Model	S_{cdf}	Optimized parameters	Parameter bounds	Number of wolves	Number of generations
Bézier 2-fold	0.018900	[0.02, 0.865945, 0.871320]	[[0.02, 0.02] cm, [0, 1], [0, 1]]	80	500
Bézier 3-fold	0.000417	[0.02, 4.345357e-04, 7.484435e-01, 9.662662e-01]	[[0.02, 0.02] cm, [0, 1], [0, 1], [0, 1]]	80	500
Free harmonic holes	0.047874	[5.000000e-04, 2.000000e+00, 3.000000e-03, 7.000000e-03, 3.000000e-03, 5.793045e-01, 0.000000e+00, 9.532601e-03, 1.643613e-01, 4.204582e-01, 4.711165e-02, 2.656237e-02, 4.022482e-01, 6.500855e-02, 5.192538e-01, 7.000000e-03, 4.461367e-03, 3.000000e-03, 1.000000e+00, 1.515416e-01, 4.651967e-02, 1.019129e-01, 2.235705e-02, 7.957423e-03, 3.416316e-03, 1.537801e-03, 7.284446e-01, 7.893828e-01]	$w = 0.05$ cm, 2 holes, $(x, y) \in [0.3, 0.7]$ cm, $R_{max} \in [0.05, 0.3]$ cm, $\forall k \in [1, 5] (c_k, \phi_k) \in [0, 1]^2$	500	500

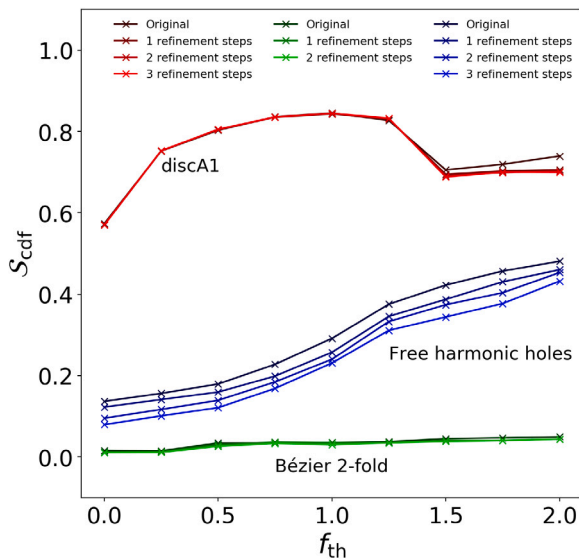


Fig. D.9. Numerical stability of stress diversity metric evaluated across specimen designs. The red line represents simple disc hole (Fig. 2 d-f), green line represents optimized hole arrays with 2-fold symmetry (Fig. 4 a-c), and blue line for the optimized free harmonic hole (Fig. 4 g-i). The stress diversity metric was assessed for varying f_{th} values ranging from 0 to 2.0. Mesh refinement, with a minimum feature size of approximately 3×10^{-4} of the sample width, was performed until exceeding 100,000 mesh cells. (For interpretation of the references to color in this figure legend, the reader is referred to the web version of this article.)

References

- [1] H. Czychos, T. Saito, L. Smith, *Springer Handbook of Materials Measurement Methods*, vol. 978, Springer, 2006.
- [2] A. International, *ES/ESM-16a: Standard Test Methods for Tension Testing of Metallic Materials*, ASTM international, 2016.
- [3] J.R. Davis, *Tensile Testing*, ASM international, 2004.
- [4] R. Hill, J. Rice, Constitutive analysis of elastic-plastic crystals at arbitrary strain, *J. Mech. Phys. Solids* 20 (6) (1972) 401–413.
- [5] R. Hill, *The Mathematical Theory of Plasticity*, vol. 11, Oxford University Press, 1998.
- [6] A. Argon, *Strengthening mechanisms in crystal plasticity*, vol. 4, OUP Oxford, 2007.
- [7] K. Rao, E. Hawbolt, Development of constitutive relationships using compression testing of a medium carbon steel, *J. Eng. Mater. Technol.* 114 (1) (1992) 116–123.
- [8] T. Hoc, J. Crépin, L. Gélébart, A. Zaoui, A procedure for identifying the plastic behavior of single crystals from the local response of polycrystals, *Acta Mater.* 51 (18) (2003) 5477–5488.
- [9] E. Plancher, V. Favier, C. Maurice, E. Bosso, N. Rupin, J. Stodolna, D. Loizard, J.-B. Marijon, J. Petit, J.-S. Micha, et al., Direct measurement of local constitutive relations, at the micrometre scale, in bulk metallic alloys, *J. Appl. Crystallogr.* 50 (3) (2017) 940–948.
- [10] T. Kirchdoerfer, M. Ortiz, Data-driven computational mechanics, *Comput. Methods Appl. Mech. Engrg.* 304 (2016) 81–101.
- [11] R. Eggersmann, T. Kirchdoerfer, S. Reese, L. Stainier, M. Ortiz, Model-free data-driven inelasticity, *Comput. Methods Appl. Mech. Engrg.* 350 (2019) 81–99.
- [12] R. Ibañez, D. Borzacchiello, J.V. Aguado, E. Abisset-Chavanne, E. Cueto, P. Ladeveze, F. Chinesta, Data-driven non-linear elasticity: constitutive manifold construction and problem discretization, *Comput. Mech.* 60 (2017) 813–826.
- [13] D. Chen, D.I. Levin, S. Sueda, W. Matusik, Data-driven finite elements for geometry and material design, *ACM Trans. Graph.* 34 (4) (2015) 1–10.
- [14] K. Ciftci, K. Hackl, Model-free data-driven simulation of inelastic materials using structured data sets, tangent space information and transition rules, *Comput. Mech.* 70 (2) (2022) 425–435.
- [15] S.K. Mitusch, S.W. Funke, M. Kuchta, Hybrid FEM-NN models: Combining artificial neural networks with the finite element method, *J. Comput. Phys.* 446 (2021) 110651.
- [16] Y. Zhang, Q.-J. Li, T. Zhu, J. Li, Learning constitutive relations of plasticity using neural networks and full-field data, *Extreme Mech. Lett.* 52 (2022) 101645.
- [17] M. Fläschel, S. Kumar, L. De Lorenzis, Discovering plasticity models without stress data, *npj Comput. Mater.* 8 (1) (2022) 1–10.
- [18] T. Chu, W. Ranson, M.A. Sutton, Applications of digital-image-correlation techniques to experimental mechanics, *Exp. Mech.* 25 (3) (1985) 232–244.
- [19] E. Barnard, L. Wessels, Extrapolation and interpolation in neural network classifiers, *IEEE Control Syst. Mag.* 12 (5) (1992) 50–53.
- [20] P. Haley, D. Soloway, Extrapolation limitations of multilayer feedforward neural networks, in: [Proceedings 1992] IJCNN International Joint Conference on Neural Networks, vol. 4, 1992, pp. 25–30, <http://dx.doi.org/10.1109/IJCNN.1992.227294>.
- [21] H. Lohninger, *Teach/me: Data Analysis*, Springer, 1999.
- [22] W. Waldman, M. Heller, G. Chen, Optimal free-form shapes for shoulder fillets in flat plates under tension and bending, *Int. J. Fatigue* 23 (6) (2001) 509–523.
- [23] J. Rezaeepazhand, M. Jafari, Stress concentration in metallic plates with special shaped cutout, *Int. J. Mech. Sci.* 52 (1) (2010) 96–102.
- [24] M.T. Ozkan, I. Toktas, Determination of the stress concentration factor (Kt) in a rectangular plate with a hole under tensile stress using different methods, *Mater. Test.* 58 (10) (2016) 839–847.
- [25] P. Romanowicz, A. Muc, Estimation of notched composite plates fatigue life using residual strength model calibrated by step-wise tests, *Materials* 11 (11) (2018) 2180.
- [26] P.J. Romanowicz, B. Szybiński, M. Wygoda, Application of DIC method in the analysis of stress concentration and plastic zone development problems, *Materials* 13 (16) (2020) 3460.
- [27] L. Euler, *Formulae generales pro translatione quacunque corporum rigidorum*, *Novi Commentarii Acad. Sci. Petropolitanae* (1776) 189–207.
- [28] M. Yu, M. Yu, M.-H. Yu, *Unified Strength Theory and Its Applications*, Springer, 2004, pp. 33–34.
- [29] R.W. Cahn, P. Haasen, *Physical Metallurgy*, vol. 1, Elsevier, 1996.
- [30] R. von Mises, *Mechanik der festen körper im plastisch-deformablen zustand*, *Nachrichten von Gesellschaft Wissenschaften zu Göttingen, Math.-Phys. Kl.* 1913 (1913) 582–592.
- [31] J. Li, P.G. Kevrekidis, C.W. Gear, I.G. Kevrekidis, Deciding the nature of the coarse equation through microscopic simulations: The baby-bathwater scheme, *SIAM Rev.* 49 (3) (2007) 469–487.
- [32] M.S. Alnaes, J. Blechta, J. Hake, A. Johansson, B. Kehlet, A. Logg, C. Richardson, J. Ring, M.E. Rognes, G.N. Wells, The FEniCS project version 1.5, *Arch. Numer. Softw.* 3 (2015) <http://dx.doi.org/10.11588/ans.2015.100.20553>.
- [33] J. Lemaitre, Coupled elasto-plasticity and damage constitutive equations, *Comput. Methods Appl. Mech. Engrg.* 51 (1–3) (1985) 31–49.
- [34] C. Allen, B. Boardman, *ASM handbook, volume 1, properties and selection: irons, steels, and high performance alloys section: publication information and contributors publication information and contributors*, Fonderie 1 (2005) 1051.
- [35] *Steels, general properties, 2022*, <https://www.matweb.com/search/datasheet.aspx?matguid=10e1c14130cd4ed6ae64b85723be53af>.
- [36] M.I. Radaideh, K. Du, P. Seurin, D. Seyler, X. Gu, H. Wang, K. Shirvan, NEORL: NeuroEvolution optimization with reinforcement learning, 2021, arXiv preprint arXiv:2112.07057.
- [37] S. Mirjalili, S.M. Mirjalili, A. Lewis, Grey wolf optimizer, *Adv. Eng. Softw.* 69 (2014) 46–61.
- [38] S. Ruder, An overview of gradient descent optimization algorithms, 2016, arXiv preprint arXiv:1609.04747.
- [39] A. Clausen, F. Wang, J.S. Jensen, O. Sigmund, J.A. Lewis, Topology optimized architectures with programmable Poisson's ratio over large deformations, *Adv. Mater.* 27 (37) (2015) 5523–5527.
- [40] E. Cerda, L. Mahadevan, Geometry and physics of wrinkling, *Phys. Rev. Lett.* 90 (7) (2003) 074302.
- [41] D. Steigmann, Tension-field theory, *Proc. R. Soc. Lond. Ser. A Math. Phys. Eng. Sci.* 429 (1876) (1990) 141–173.
- [42] A.C. Kak, M. Slaney, *Principles of Computerized Tomographic Imaging*, SIAM, 2001.
- [43] A.C. Bovik, *Handbook of Image and Video Processing*, Academic Press, 2010.
- [44] T. Hahn, U. Shmueli, J.W. Arthur, *International Tables for Crystallography*, vol. 1, Reidel Dordrecht, 1983.
- [45] D. Schattschneider, The plane symmetry groups: their recognition and notation, *Amer. Math. Monthly* 85 (6) (1978) 439–450.
- [46] R.H. Bartels, J.C. Beatty, B.A. Barsky, *An Introduction to Splines for Use in Computer Graphics and Geometric Modeling*, Morgan Kaufmann, 1995.